On Viscosity and Density Affecting Aeroelasticity of ONERA M6 Wing from Subsonic to Transonic Regimes

Stefan Nilsson,[1,2] Hua-Dong Yao,[1] Anders Karlsson,[2] and Sebastian Arvidson[1,2]

[1)] *Department of Mechanics and Maritime Sciences, Chalmers University of Technology, Gothenburg, Sweden*

[2)] *SAAB AB, Aeronautics, SE-581 88, Linköping, Sweden*

(*Electronic mail: stefnil@chalmers.se)

The effects of fluid viscosity and density on the aeroelasticity of the ONERA M6 wing over a wide range of free-stream Mach numbers, spanning 0.6–1.1, based on viscous and inviscid flow assumptions are studied. Both static and dynamic responses of the wing are examined. We employ a hybrid Reynolds-Averaged Navier-Stokes (RANS) and Large-Eddy Simulation (LES) method for the viscous flow, namely Delayed Detached-Eddy Simulation (DDES) with the Spalart-Allmaras (SA) turbulence model. The inviscid flow solver uses the Euler equations. A few selected cases are also analysed using Unsteady RANS (URANS). The flow solvers are strongly coupled to a structural analysis software, which uses a modal formulation. The structural responses are analysed using a constant free-stream density for all Mach numbers. In addition, higher densities are used for all Mach numbers in order to find the critical dynamic pressure where flutter is obtained. A substantial difference in the aeroelastic responses is found for Mach numbers ranging 0.875–0.95, when comparing viscous and inviscid flow simulations. Furthermore, it is shown that viscosity is of minor importance at subsonic and supersonic speeds. At Mach number 0.8395 it is shown that DDES provides close to identical structural responses as URANS. The largest difference of the predicted flutter boundaries is found in the transonic region. The flutter boundary for viscous flow stands out at Mach 0.925 where it is 53% higher than the flutter boundary predicted by inviscid flow. Simulations with URANS showed that it would predict a lower flutter boundary at Mach 0.925, compared to DDES.

I. INTRODUCTION

Transonic flows feature strong nonlinear mechanisms, which are detrimental to the aeroelastic behaviour of lifting surfaces. Fluid viscosity plays an important role in affecting the flow nonlinearity, especially in transonic flows where non-isentropic effects exist and shock waves interact with boundary layers. At subsonic and supersonic speeds when the flow is fully isentropic around a lifting surface, it is often adequate to assume inviscid fluids for aeroelastic prediction. However, this assumption is not valid for transonic flows, leading to inaccurate prediction of shock wave locations. Aside from the viscosity, the density and flow speed determine the dynamic pressure, which governs aeroelastic flutter.

In Shock Wave/Boundary-Layer Interaction (SWBLI)[1] phenomena including flow separation, the flow in a boundary layer is always subsonic near the wall, and an adverse pressure gradient moves upstream towards the subsonic part of the boundary layer[1]. The aerodynamic forces and moments are sensitive to the shock wave position due to the strong pressure gradient across the shock wave. Moreover, shock waves are in many cases non-stationary, not only due to unsteady flow but also due to local changes of the Angle of Attack (AOA), caused by the aeroelastic deformation. The effects of unsteady aerodynamics in the transonic region make accurate aeroelastic prediction most challenging[2].

Aeroelasticity can be divided into two categories: static and dynamic aeroelasticity[3]. The static aeroelasticity refers to the state where there is equilibrium between aerodynamic forces and elastic forces. The interaction is bidirectional since a change in the aerodynamic forces affects the structural deformation and vice versa. This is also true for the dynamic aeroelasticity. The static aeroelasticity is fundamental for structural integrity, and the static stability is a prerequisite for the dynamic stability.

The dynamic aeroelasticity embodies aerodynamics, elasticity, and dynamics. Flutter is one of the most renown phenomena associated with the dynamic aeroelasticity. The flutter is a self-excited oscillatory instability in which the aerodynamic forces couple with elastic body's natural oscillatory modes. If the flutter commences, the amplitudes of structure oscillations will increase with time[4]. Thus, the flutter can swiftly cause complete failure of an airframe. The flutter boundary indicates the onset of the dynamic instability, which is governed by the dynamic pressure. An aeroplane flying at low altitude and high speed often verges upon the flutter boundary. Furthermore, a wing is often more susceptible to the flutter at transonic speeds[4]. The flutter boundary is usually lower at transonic speeds than at subsonic and supersonic speeds. As can be seen, the instability is dependent on the air density changing with altitudes and flight speeds.

Since the flutter is detrimental to an airframe, it must always be ascertained that an aircraft never encounters flutter conditions. Theories and methodology on fluid-structure interaction (FSI) are therefore important to the aerospace industry. Extensive flight-testing campaigns that involve some risks are necessary. The risk and the extent of flight-testing could be reduced by the utilisation of more sophisticated numerical methods. It is commonplace to use linear methods or inviscid flow solvers for aeroelastic analyses, due to their comparatively low computational cost. However, the inviscid assumption and linear methods are usually not adequate for the transonic flows. In wind tunnel testing of aeroelastic applications, the model scaling might be problematic and affect the testing validity. Furthermore, the flow over a down-scaled model also suffers from scaling effects. For instance, boundary-layer growth, and the location of the transition from laminar to turbulent boundary-layer are affected. This can further lead to changes in the positions of shock waves. The scaling effects are often most significant close to, or with mild, flow separation[5]. In contrast to the wind tunnel testing of down-scaled models, full-scale aircraft configurations can be evaluated using numerical simulations.

A paper by Heeg et al.[2] , collates the main findings of the AIAA Aeroelastic Prediction Workshop, held in 2012. The purpose of the workshop was to assess state-of-the-art computational aeroelasticity methods. Three aeroelastic wing configurations in transonic flow were used as the basis for the workshop. The three configurations were examined by different research teams, using their preferred computational tools; Reynolds-Averaged Navier-Stokes (RANS) equations based methods were opted for by most teams. Comparisons with experimental data showed that, in cases with fully attached flow, the RANS methods were able to predict aeroelastic behaviour sufficiently. However, in cases with separated flow, they concluded that Unsteady RANS (URANS) was not sufficient to capture the aeroelastic behaviour, although the flow separation was moderate in these cases. The use of URANS for cases with mild, or incipient separation may lead to erroneous aeroelastic predictions.

Durrani and Qin[6] examined the performance of Detached-Eddy Simulation (DES), Delayed DES (DDES), and URANS in conjunction with the Spalart-Allmaras (SA) turbulence model[7,8], on the rigid ONERA M6 wing at Mach 0.8395 with an AOA of 3.06 degrees. They reported a good comparison regarding pressure distribution in relation to the experimental data. However, at higher Mach numbers, and also due to aeroelastic deformation, there might be significant differences to the case studied by Durrani and Qin. At higher transonic Mach numbers, the shocks can be expected to be stronger. Moreover, aeroelastic deformation alters local AOA. These two factors increase the risk of flow separation, which motivates the choice of the SA-DDES turbulence model in lieu of the SA-URANS model.

In this paper we utilise SA-DDES[8] to study the influence of viscous effects and density on aeroelastic prediction of the ONERA M6 wing[9]. The wing aeroelasticity at Mach numbers spanning from 0.6–1.1 are investigated, given constant static free-stream pressure, density, and temperature, as well as a constant AOA of 3.06 degrees. To address the viscosity effects, inviscid flow simulations based on the inviscid Euler equations (IEE) are also performed. A few selected cases are simulated with URANS for the methodology comparison purpose. Both static and dynamic structural responses are examined. Furthermore, all Mach numbers are simulated with higher static densities (increased dynamic pressure) in order to find the flutter boundary.

The forthcoming section introduces the numerical methods. Followed by the computational setup, which includes the descriptions of the wing geometry, the structural model, free-stream conditions, as well as boundary and initial conditions. The computational setup section also includes the results from a grid convergence study and flow solver validation performed using the rigid wing. The following section presents the results from aeroelastic simulations. The paper concludes with a summation of the most important findings.

II. NUMERICAL METHODS

The flow/structural solver M-Edge[10,11] is used for all flow and structural simulations. It incorporates both a Navier-Stokes flow solver, an IEE flow solver, and a modal solver for the structural analysis.

A. Method for flow simulation

The unstructured flow solver M-Edge uses an edge-based formulation and a node centred finite-volume method to discretise the governing equations. A second order central difference scheme, with Jameson type scalar artificial dissipation, is employed for spatial discretisation of the momentum equation. A second order backward differencing scheme, together with a dual-time stepping methodology, which uses a fully implicit steady-state time marching scheme, are used for time integration. For the viscous simulation, DDES and URANS based on the Spalart-Allmaras one-equation model are used[7,8] in conjunction with a wall function[12].

B. Method for structural simulation

The modal formulation is based on the eigenvalue problem of the full structural model and provides a set of linear equations describing structural deformation. The time dependent structural coordinate $x(t)$ is given by the structural dynamics equation:

$$\boldsymbol{M}\ddot{x}(t) + \boldsymbol{C}\dot{x}(t) + \boldsymbol{K}x(t) = f(t), \tag{1}$$

$$\boldsymbol{C} = \alpha \boldsymbol{M} + \beta \boldsymbol{K}, \quad \alpha, \beta \geq 0. \tag{2}$$

Here $\boldsymbol{M}$ is the mass matrix, $\boldsymbol{K}$ is the stiffness matrix, and $\boldsymbol{C}$ is the Rayleigh damping matrix. $\boldsymbol{M}$, $\boldsymbol{K}$, and $\boldsymbol{C}$ are real and symmetric. The time dependency of the structural coordinate $x(t)$ is represented by normal mode shapes ϕ_k and modal coordinates $q_k(t)$:

$$x(t) = x_0 + \sum_{k=1}^{N_m} q_k(t)\phi_k. \tag{3}$$

The subscript k indicates the k-th mode, and x_0 is the initial condition, $x_0 = x(t=0)$. For the special case of free vibration, the external forces and the damping are both zero, the equation of motion, Eq.(1), reduces to a generalised eigenvalue problem:

$$\boldsymbol{K}\phi_k = \omega_k^2 \boldsymbol{M}\phi_k, \quad k \in [1, N]. \tag{4}$$

The solution to the eigenvalue problem gives a set of eigenvectors, i.e., the normal mode shapes ϕ_k. The corresponding eigenvalues are treated in terms of angular frequencies ω_k. N is equal to the dimension of x, which is the aggregated number of structural degrees of freedom. It is assumed that the normal mode shapes and corresponding frequencies are ordered as $\omega_1 < \omega_k < \omega_{k+1} <, \cdots, < \omega_{N-1} < \omega_N$. It can be shown that the normal mode shapes satisfy the orthogonality conditions:

$$\phi_j^T \boldsymbol{M}\phi_k = a_k \delta_{jk}, \tag{5}$$

$$\phi_j^T \boldsymbol{K}\phi_k = a_k \omega_k^2 \delta_{jk}. \tag{6}$$

Here the normalisation constant a_k is known as the generalised mass for the k-th mode, and δ is the Kronecker delta function. The full system with N degrees of freedom can easily be truncated at order $N_m \ll N$. With the use of the truncated modal basis, the structural dynamics equation, Eq. (1), can be reduced to a set of N_m scalar equations, which are coupled only through the external force term. Using Eq. (3) and the orthogonality conditions (Eqs. (5) and (6)), and pre-multiplying Eq. (1) with the transpose of ϕ_k, the equation of motion can be rewritten as:

$$a_k \ddot{q}_k + 2\zeta_k a_k \omega_k \dot{q}_k + a_k \omega_k^2 q_k = Q_k, \quad k \in [1, N_m], \tag{7}$$

$$Q_k = \phi_k^T f. \tag{8}$$

Here ζ_k is the damping ratio for mode k, and Q_k is known as the generalised force[10]. A Newmark's time-integration scheme is applied to Eq. (7):

$$\dot{q}_k^{n+1} = \dot{q}_k^n + \Delta t(1-\gamma)\ddot{q}_k^n + \Delta t \gamma \ddot{q}_k^{n+1}, \tag{9}$$

$$q_k^{n+1} = q_k^n + \Delta t \dot{q}_k^n + \Delta t^2 \left(\frac{1}{2} - \sigma\right) \ddot{q}_k^n + \Delta t^2 \sigma \ddot{q}_k^{n+1}. \tag{10}$$

Here Δt is the time step and n is the time step number. Setting the parameters $\gamma = \frac{1}{2}$ and $\sigma = \frac{1}{6}$ corresponds to a linear interpolation of the modal acceleration $\ddot{q}(t), t \in [t^n, t^{n+1}]$. Combining Eq. (7), (9) and (10), the modal acceleration $\ddot{q}_k^{n+1}$ can be computed. Subsequently, the acceleration can be substituted back into Eqs. (9) and (10) which gives the modal velocity and coordinate. Applying a damping ratio of unity, i.e., critical damping, to the structure in a FSI simulation is useful to ramp-up the convergence pace, when static deformation is sought. Given an oscillatory signal, the damping ratio ζ can be computed from:

$$\varepsilon = \frac{1}{n} \ln\left(\frac{Y_0}{Y_n}\right), \tag{11}$$

$$\zeta = \frac{\varepsilon}{\sqrt{4\pi^2 + \varepsilon^2}}. \tag{12}$$

Here ε is the logarithmic decrement and Y is the peak amplitude of the n-th period[13].

III. COMPUTATIONAL SETUP

This section introduces the geometry, ensued by a description of the structural FE model and its modal representation. The following paragraph introduces all studied flow cases, along with boundary and initial condition. The section concludes with a description of the computational fluid dynamics (CFD) grids along with results from the flow solver validation. A grid convergence study is also undertaken using steady RANS, the results from this study are also presented in the last paragraph.

A. Geometry

The ONERA M6 wing[9] is a swept, low aspect ratio wing with a symmetric aerofoil that has been utilised extensively in numerous research projects. The wing was originally made for wind tunnel testing and the logged data have since been used as reference and validation for flow solvers. No aeroelasticity data are available. The wingspan is 1196.3 mm and the wing-root chord length is 805.9 mm. The leading-edge sweep angle is 30 degrees, and the trailing edge sweep angle is 15.8 degrees. The original wing has a rounded wingtip, whereas the wingtip used here is flat. Some difference in comparison to experimental data is thus expected, especially adjacent to the wingtip. For further details on the geometry the reader is referred to[9].

B. Structural finite element model

The structural finite element (FE) model is shown in Figure 1. The wing's whole interior is supported. The interior support is assembled using two-dimensional quadrilateral and triangular elements. The skin of the wing consists of quadrilateral elements, except at the wing-root and wingtip where triangular elements are used. The total number of grid points is 12096. The element shell thickness is 1.0 mm, for all elements. Utilising this type of interior support results in a very stiff wing when ordinary material properties, such as aluminium, are used. The material properties are therefore tweaked such that the wing's natural frequencies are in a suitable range (see upcoming paragraph). The material properties are presented in Table I. The model is assembled from two-dimensional elements rather than three-dimensional elements, due to a limitation in the software that maps the normal mode shapes onto the CFD grid.

TABLE I. Material properties of the structural FE model.

Density [$kg \cdot m^{-3}$]	Young's modulus [$kg \cdot m^{-1}s^{-2}$]	Poisson's ratio [-]
6000	$9.0 \cdot 10^9$	0.32

C. Modal representation of the structural model

The structural eigenvalue problem is solved to obtain the modal frequencies, the generalised stiffness, and the normal mode shapes. For the aeroelastic analysis of a wing, the first bending

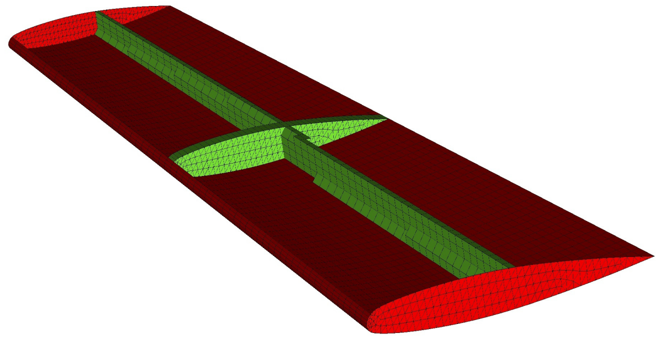

FIG. 1. Structural FE model. Cut planes (green) show a portion of the inner structure, which are assembled using two-dimensional elements.

mode and the first torsion mode of the wing are most important. Beyond that, frequencies above 100 Hz are rarely important for the analysis of an aircraft wing. Seven modes are considered in this analysis, which include the first three bending and torsion modes. The normal mode shapes are shown in Figure 2. Frequencies, generalised mass, and generalised stiffness are given in Table II. All grid points except those at the wing root have six degrees of freedom, and the constraints are applied to all degrees of freedom at the wing root. The normal mode shapes are mapped onto the CFD grid. Each mode shape is stored in a so-called perturbation grid, which is simply the CFD grid deformed to match the normal mode shape. The inclusion of additional modes has little effect on computation time. However, at higher mode numbers, the shapes become increasingly complex. For CFD grids with high Reynolds numbers, it can be problematic to perform the deformations even for the first few modes. Adding more modes exacerbates the problem, and the accuracy gained is often negligible.

D. Free-stream, boundary, and initial conditions

Nine Mach numbers ranging from 0.6 to 1.1 for different free-stream static pressure p_s and dynamic pressure p_{dyn} are studied. A static free-stream temperature of 288.15 K is set in all cases. Specifically, $p_s = 94$ kPa is simulated at all Mach numbers using both SA-DDES and IEE, to identify how the viscosity affects the simulation accuracy. Moreover, in order to find out the flutter boundary at each Mach number, p_{dyn} is changed with an increment of 11340 Pa by adjusting p_s, which is equivalent to adjusting the density ρ as the temperature is kept constant at 288.15 K. Each point on the flutter boundary derives from interpolation between the two dynamic pressures that

TABLE II. Modal frequencies, generalised mass, and stiffness.

Mode	Frequency [Hz]	Generalised mass [kg]	Generalised stiffness [Ns^{-1}]
1	7.65	1.0	2311.9
2	29.44	1.0	34212.7
3	37.73	1.0	56187.1
4	64.67	1.0	165112.0
5	71.85	1.0	203822.8
6	92.88	1.0	340600.2
7	126.14	1.0	628103.4

result in a damping ratio closest to zero, whereof one dynamic pressure gives a positiv damping ratio and the other gives a negative damping ratio. The two simulations for each Mach number with different dynamic free-stream pressures, wherefrom the flutter boundary stems are presented in this paper. A few selected cases are also simulated with SA-URANS for comparison with SA-DDES.

The free-stream conditions for all cases are presented in Table III, which also indicates which method is used for each case. Case 7 is chosen because it corresponds to the wind tunnel conditions in the experiments of Schmitt et al.[9]. The AOA in the experiment was 3.06 degrees, which is also used here for all simulations. The experimental data are used as a reference and compared with the results from CFD for the corresponding case with the rigid wing; the experiment did not encompass aeroelastic measurements because the wing was rigid.

All FSI simulations are initiated with an established flow field from transient simulations on the rigid wing. In order to find the static deformation, the damping ratio for all structural modes is set to $\zeta_k = 1$, i.e., the critical damping. The dynamic response is then simulated by setting the damping ratio to zero and applying an initial modal velocity to the first torsional mode (Mode 2). An initial modal velocity of 100 ms^{-1} is used for the cases with $p_s = 94$ kPa. For the other cases, the initial modal velocity is set to 25 ms^{-1}. By applying the disturbance to the torsional mode, the bending mode is also directly affected due to the change of the aerodynamic forces as the local AOA is altered.

A weak characteristic far-field boundary condition is used. A symmetry boundary condition is applied to the boundary where the wing root is attached, see Figure (5(a). For viscous simulations,

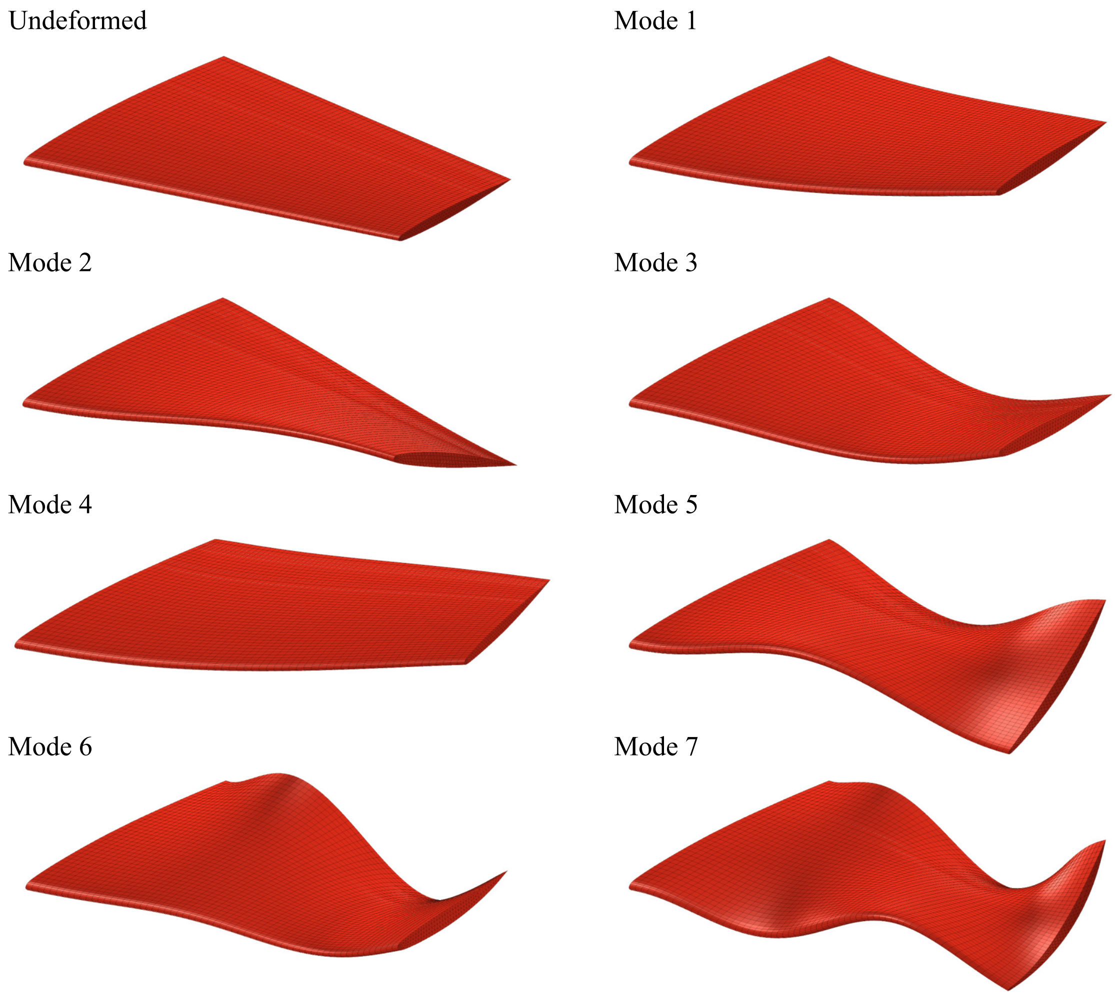

FIG. 2. The undeformed wing and the normal mode shapes: Mode 1 – 1st bending mode, Mode 2 – 1st torsional mode, Mode 3 – 2nd bending mode, Mode 4 – 1st in-plane bending mode, Mode 5 – 2nd torsional mode, Mode 6 – 3rd bending mode, Mode 7 – 3rd torsional mode.

an adiabatic, no-slip boundary condition with a wall function is used at the wing surface boundary. For inviscid flow simulations, a free-slip condition is applied to the wing surface. A time step of $2.5 \cdot 10^{-5}$ s is used for all simulations.

E. CFD grids, grid convergence and flow solver validation

A study of grid convergence is performed using three structured grids with different spatial resolutions on the wing surfaces. The number of grid points, the maximum cell edge lengths on the wing surface, and the first cell height of the coarse, medium, and fine grids are given in Table

TABLE III. Free-stream conditions. Here, I, D, and U signify whether IEE, DDES, and/or URANS simulation is performed, respectively.

Case	Method	Ma [-]	p_s [Pa]	p_{dyn} [Pa]	ρ [$\mathrm{kg \cdot m^{-3}}$]	Case	Method	Ma [-]	p_s [Pa]	p_{dyn} [Pa]	ρ [$\mathrm{kg \cdot m^{-3}}$]
1	I,D	0.6000	94000	23688	1.1367	18	I,D	0.9250	94000	56300	1.1367
2	I,D	0.6000	585000	147420	7.0738	19	I	0.9250	227202	136080	2.7473
3	I,D	0.6000	630000	158760	7.6180	20	I	0.9250	246136	147420	2.9763
4	I,D	0.8000	94000	42112	1.1367	21	D,U	0.9250	359737	215460	4.3500
5	I,D	0.8000	202500	90720	2.4486	22	D,U	0.9250	378671	226800	4.5789
6	I,D	0.8000	227812	102060	2.7547	23	I,D	0.9500	94000	59385	1.1367
7	I,D,U	0.8395	94000	46373	1.1367	24	I,D	0.9500	305152	192780	3.6899
8	I,D,U	0.8395	160906	79380	1.9457	25	I,D	0.9500	323102	204120	3.9070
9	I,D,U	0.8395	183892	90720	2.2236	26	I,D	0.9750	94000	62551	1.1367
10	I,D	0.8750	94000	50378	1.1367	27	D	0.9750	272663	181440	3.2970
11	I	0.8750	169273	90720	2.0469	28	I,D	0.9750	289704	192780	3.5031
12	I,D	0.8750	190433	102060	2.3027	29	I	0.9750	306746	204120	3.7092
13	D	0.8750	211592	113400	2.5586	30	I,D	1.1000	94000	79618	1.1367
14	I,D	0.9000	94000	53298	1.1367	31	D	1.1000	281157	238140	3.3998
15	I	0.9000	180000	102060	2.1766	32	D	1.1000	294545	249480	3.5617
16	I,D	0.9000	200000	113400	2.4184	33	I	1.1000	307934	260820	3.7235
17	D	0.9000	220000	124740	2.6602	34	I	1.1000	321322	272160	3.8854

IV. The wing surface meshes of the three grids are displayed in Figure 3. The largest elements are at the wing root, where the span-wise and chord-wise cell edge lengths are approximately equal. Toward the wing tip, the cell size naturally becomes smaller as the wing tapers. The average y^+ value ranges from 140 at Mach 0.6000 to 190 at Mach 1.1000. Higher y^+ values, up to about 300, are achieved locally, typically at the leading edge. Given the large $y+$ values, the wall function is applied in the DDES and URANS simulations. The three grids are called wall-function (WF) grids.

However, the utilisation of wall functions may impair the accuracy in shock wave regions. Hence, it is of interest to investigate their possible influences. A wall-resolved (WR) grid is gen-

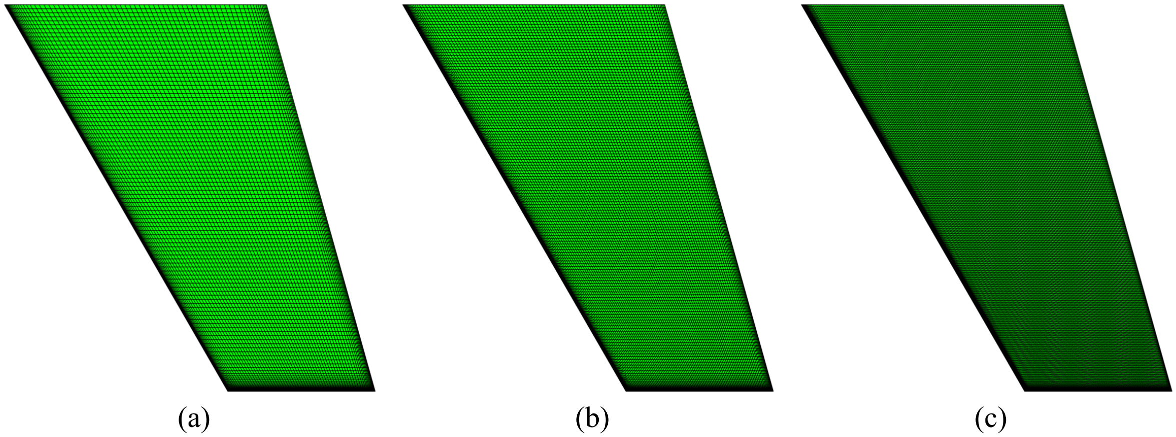

FIG. 3. Surface cells of the grids used for the grid convergence study: (a) coarse, (b) medium, (c) fine. Note that the difference between the WF, WR and IEE grids is only the wall-normal heights of the first-layer cells, but not the surface cell dimensions.

TABLE IV. The grid parameters.

Grid	Coarse	Medium	Fine	Medium	Medium
Wall treatment	WF	WF	WF	WR	IEE
No. of grid points	3265923	4760728	8659746	9560608	2824394
Max. cell edge length	15 mm	10 mm	6 mm	10 mm	10 mm
First cell height	0.3 mm	0.3 mm	0.3 mm	2 μm	5 mm

erated by refining the wall-normal heights of cells within the boundary layer based on the medium WF grid, to achieve $y^+ \approx 1$ of the first cell. This mesh is evaluated in an SA-RANS simulation. The grid parameters are given in Table IV.

For all IEE simulations, the grid is generated by coarsening the wall-normal heights of near-wall cells based on the medium WF grid, whose parameters are given in Table IV. The cells in a cross section of the wing at the wing root are shown for of the medium WF and IEE meshes in Figure 4.

All grids are generated within the same computational domain, as illustrated in Figure 5(a). The distance between the wing and far-field boundaries are approximately 20 times the wingspan in all directions. As can be seen in Figure 5(b), the wing tip in the present study is flattened, whereas the original geometry of the wing tip is rounded. The changed geometry can alter vortices induced from the tip, so minor deviations of the simulation results compared to the experimental data are

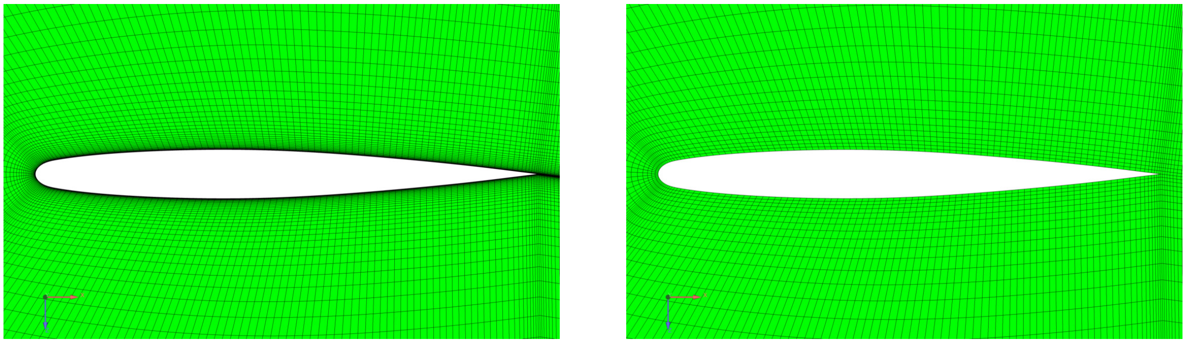

(a) (b)

FIG. 4. Cells in the cross section at the wing-root. (a) The medium WF grid. (b) The medium IEE grid.

to be expected. This is explained in more detail in the following discussion.

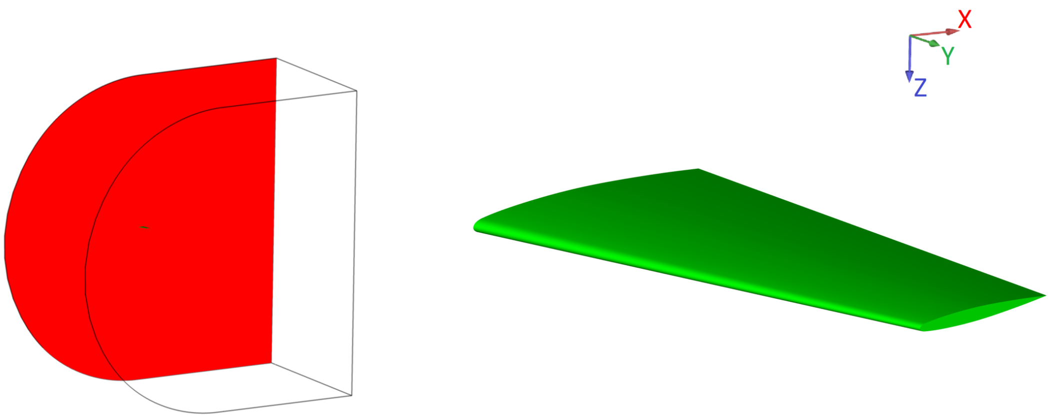

(a) (b)

FIG. 5. (a) The computational domain. The wing is attached to the symmetry plane in red. (b) The ONERA M6 wing with the low-pressure surface exposed.

The grid convergence study for the WF and WR grids is performed using the steady RANS under the flow conditions of Case 7 (see Table III). The surface pressure coefficients from these simulations, along with the corresponding experimental data[9], are shown in Figure 6. The wingspan position is measured from the wing root and is normalised based on the total wingspan length. In the streamwise direction, the distance from the leading edge, x, is normalised by the local chord length C. The difference in the pressure distribution between the WF and WR grids is found relatively small, except for the wingspan position in the range of the 90–95% wingspan, where the pressure increase corresponding to the shock wave on the suction side is more accurately predicted with the WR grid compared to the experimental data. In the range of 95–99% wingspan near the wing tip, the results of all grids differ from the experimental data for $x/C > 0.2$ downstream of the shock wave in the streamwise direction. The differences are caused by the geometry change of the wing tip, which is flattened in the present study.

The lift and drag coefficients, C_l and C_d, of the WF and WR grids with the steady RANS are presented in the upper sub-table in Table V. The lift coefficient of the WR grid is only 0.37% smaller than those of the WF grids. The difference of the drag count is 2, which is also small enough to be accepted. The small differences between the WR and WF grids in Fig 6 and Table V demonstrate that the wall function adopted in the steady simulations is valid for the use of coarse cells near the wing wall.

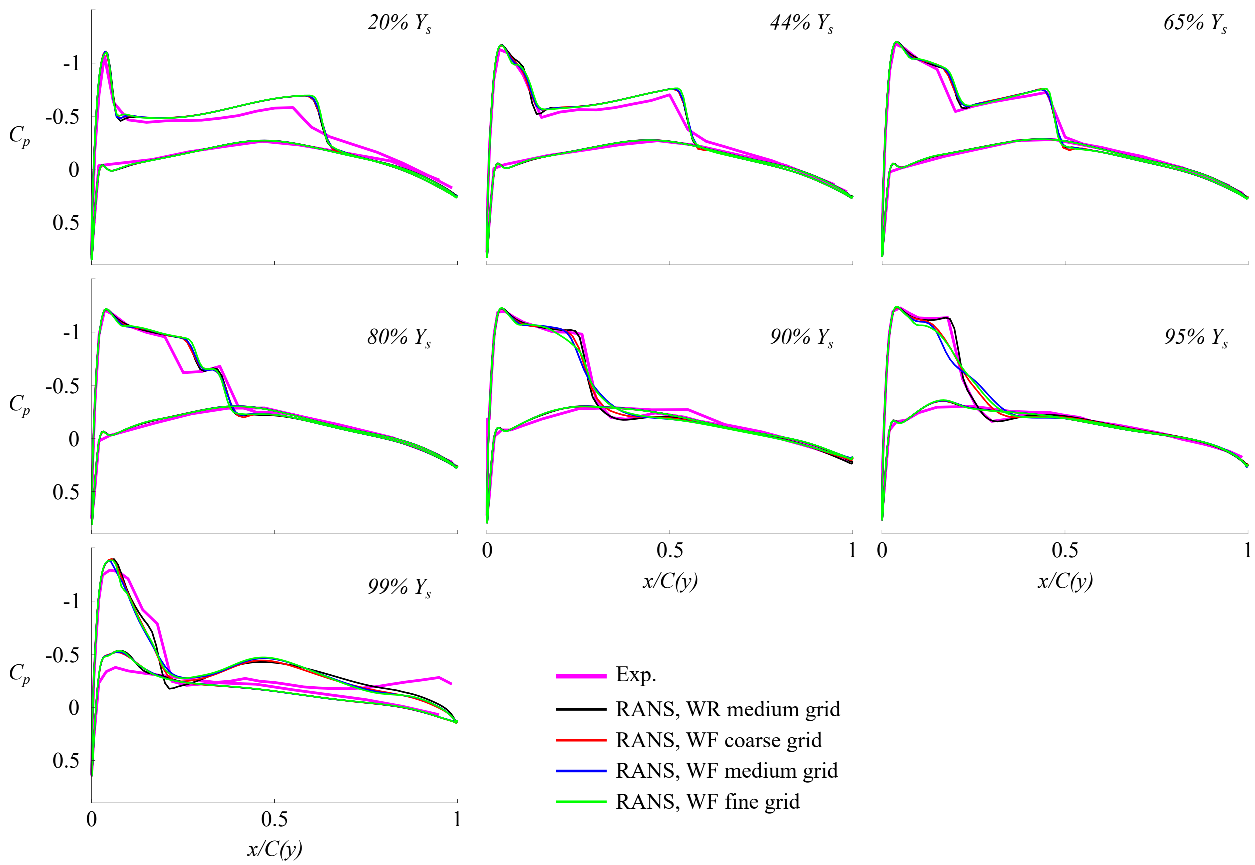

FIG. 6. The surface pressure coefficients along the the wingspan, where the total length of the wingspan is Y_s and the local chord lenght is $C(y)$. WF indicates the WF grids, for which the wall function is used.

Furthermore, the unsteady methods (IEE, URANS, and DDES) are validated based on the medium IEE and WF grids (see the grid parameters in Table IV. The flow conditions of Case 7 are adopted here. The time-averaged surface pressure coefficients are shown in Figure 7. The results of URANS show similar gradual pressure increase over the shocks compared to the steady RANS,

TABLE V. The lift and drag coefficients (C_l and C_d) predicted with the different meshes. Time-averaged results are presented for the unsteady simulation methods such as IEE, URANS and DDES.

Method	RANS WR	RANS WF	RANS WF	RANS WF
Grid	Medium	Coarse	Medium	Fine
C_l	0.269	0.271	0.272	0.273
C_d	0.0172	0.0170	0.0170	0.0170

Method	IEE	URANS WF	DDES WF
Grid	Medium	Medium	Medium
C_l	0.292	0.271	0.272
C_d	0.0124	0.0169	0.0171

whilst the DDES results align with the experimental data. It is interesting that these unsteady methods adopt the same WF mesh as the steady RANS, and all methods employ the same wall function. Therefore, the unsteadiness introduced by the LES part of DDES is beneficial to capture the shock wave.

The IEE results are observed with delayed shock wave positions across the wingspan, namely, the shock wave is situated slightly further downstream in comparison to URANS and DDES and the experimental data, as seen in Figure 7. Since the viscosity terms are not included in IEE but in URANS and DDES, the observations suggest that the viscosity affects the shock wave formation and consequently the pitching moment, which is instrumental to aeroelastic prediction.

Like the steady RANS results in Figure 6, at the 99% wingspan, all these unsteady methods exhibit deviations from the experiments in the streamwise direction in the range of $x/C > 0.2$, which is downstream of the shock wave. This can be explained because of the altered wingtip geometry.

The lift and drag coefficients predicted with the unsteady methods are listed in Table V. Compared with the steady RANS with the WF and WR grids, IEE obviously overestimates the lift coefficient but underestimates the drag coefficient, while URANS and DDES provide nearly the same prediction. Recalling the grid quality shown in Fig 4, the large discrepancies should be associated with the poor near-wall resolution of the IEE grid. Moreover, the inviscid assumption also leads to an incorrect prediction of the boundary layer, which interacts with the shock wave.

As discussed above, once the wall function is used, all WF grids adopted in the viscous flow simulations in the present study satisfactorily capture the pressure distribution and aerodynamic forces. Although the unsteady effects are not resolved in the steady RANS, the results of this approach agree with URANS and DDES. And all viscous flow simulations provide consistent predictions compared to the experiments. Therefore, the medium WF grid is used in the following presentation of the results and analysis.

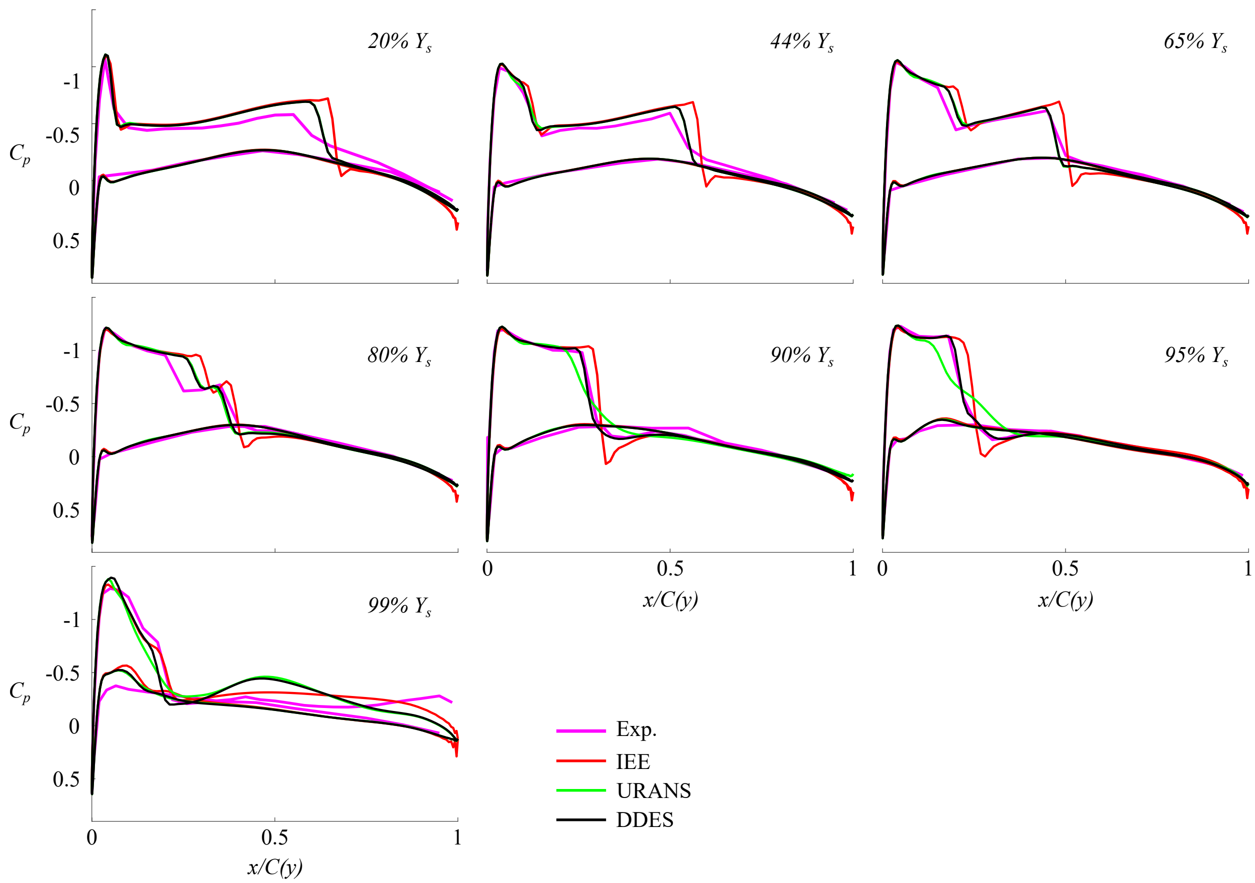

FIG. 7. The time-averaged surface pressure coefficients at 20–99% of the wingspan Y_s, computed using the unsteady methods. Here C_y is the local chord length of the wing section.

IV. RESULTS AND ANALYSIS

This section is divided into three subsections. First, the results from the simulations with constant free-stream density and static pressure $p_s = 94$ kPa using DDES and IEE are discussed. The second subsection presents the results of the flutter prediction, for which DDES and IEE are used. The third subsection presents a comparison between DDES, URANS and IEE. The structure is analysed in terms of pitch and plunge deformations. The pitch deformation is defined as the rotation of the wingtip about the axis of rotation of the first torsional mode. For clarity, the positive pitch means an increase in AOA. The plunge deformation is defined as the displacement of the torsional axis in the z-direction at the wingtip.

A. Static and dynamic responses at a constant free-stream density and pressure

Figure 8 shows the plunge and pitch deformations of the wing structural responding to a constant free-stream static pressure of 94 kPa, which are simulated using IEE and DDES. The static responses are computed from the beginning and until convergence achieved at $t = 0.25s$. Subsequently, the dynamic responses are computed till $t = 1.25s$. The viscous term of the flow is excluded from IEE but included in DDES. In other words, physically speaking, the flow simulated with IEE is inviscid, whereas that with DDES is viscous. The simulation results evince the significance of viscous effects for aeroelastic prediction at transonic speeds, both in regard to static and dynamic responses. For the plunge deformations, the effects are significant at the Mach numbers 0.8750–0.9500, whereas a minor effect can be seen for Mach numbers $Ma = 0.8000$ and 0.8395. At Ma of 0.6000, 0.9750, and 1.100, the plunge responses virtually coincide, implying that viscosity has minor influence at subsonic as well as at supersonic speeds. The inviscid flow gives a dip in the plunge damping that spans the entire transonic region, whilst the viscous flow rather gives an increased damping at most Mach numbers in the transonic region. The pitch damping for the inviscid and viscous flow are similar, except at Mach numbers 0.9250 and 0.9500 where the inviscid flow clearly gives lower damping. It is to be mentioned that the damping estimate in some cases significantly depends upon which portion of the signal is used. For a few cases, the pitch frequency shifts from the high (pitch) frequency to the low plunge frequency, for instance at $Ma = 0.8000$.

In Figure 9, the static amplitudes, characteristic frequencies and damping ratios of the plunge and pitch deformations are shown as function of Mach number. The static amplitudes are counted at time 0.25 s when the static simulations are converged, as displayed in Figure 8. The frequencies are found by computing the power spectral density (PSD) of the time signals of the dynamic responses. The damping ratio are estimated based on Eqs. (11) and (12), and the average logarithmic decrement of the initial part of the dynamic responses are considered in the estimation.

As can be seen in Figure 9, the plunge and pitch static behaviours, frequencies, and damping

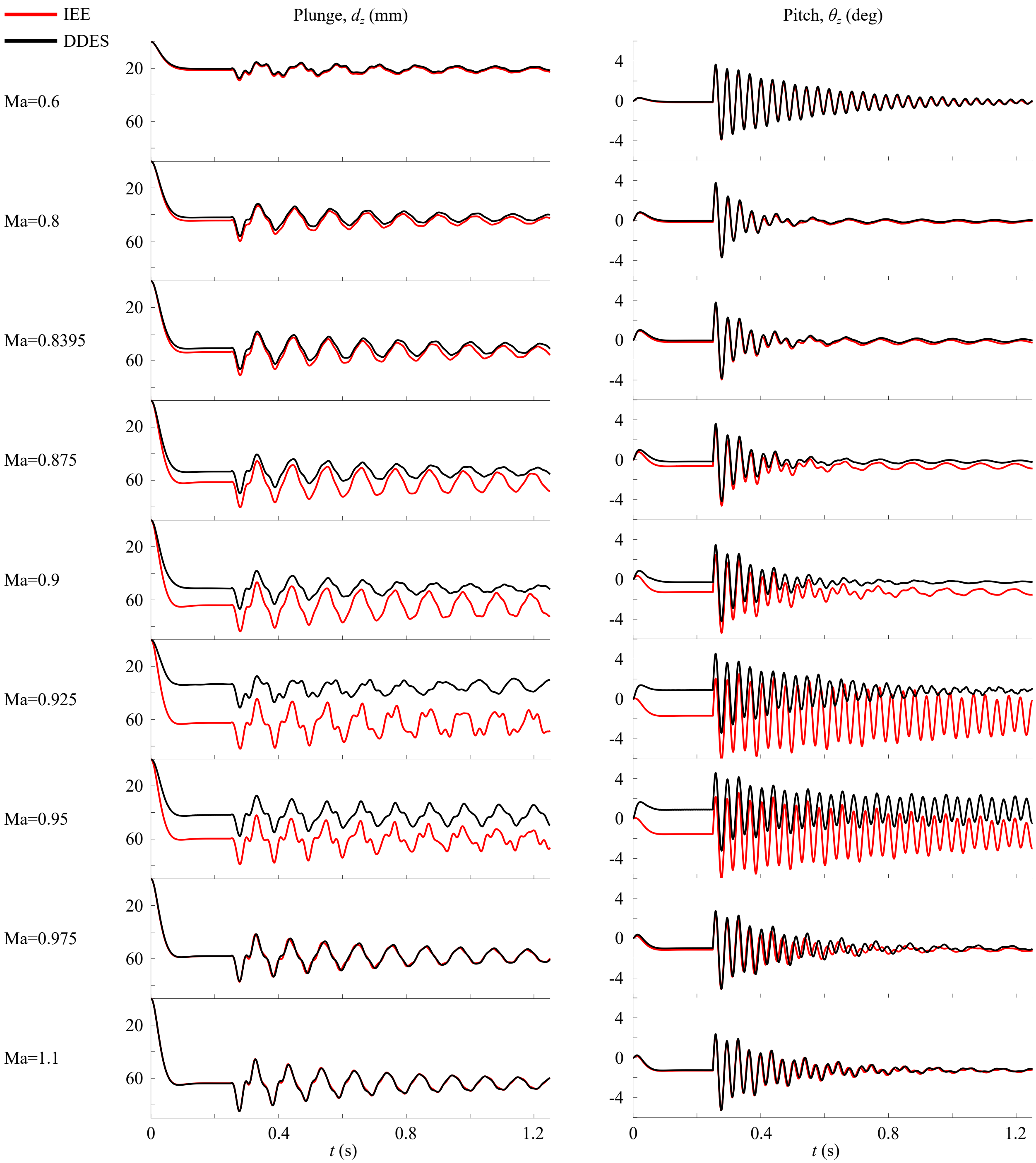

FIG. 8. Static (in $0 < t < 0.25$ s) and dynamic (in $0.25 < t < 1.25$ s) plunge and pitch responses for inviscid IEE and viscous DDES flow simulations at Mach numbers 0.6–1.1 at a constant free-stream static pressure of 94 kPa.

effects are strongly influenced by the occurrence of the shock wave in the transonic range between $Ma = 0.8 - 0.975$. The plunge frequency generally increases with the Mach number. A drop of the characteristic frequency is present at $Ma = 0.925$ in the viscous flow, which relates to the increased damping ratio. The lowest pitch frequency is found at Mach 0.8, where the highest damping ratio also is found. The plunge and pitch frequencies, which are computed based on the dynamic structural responses, also show a minor difference between the inviscid and viscous flow for subsonic and supersonic speeds.

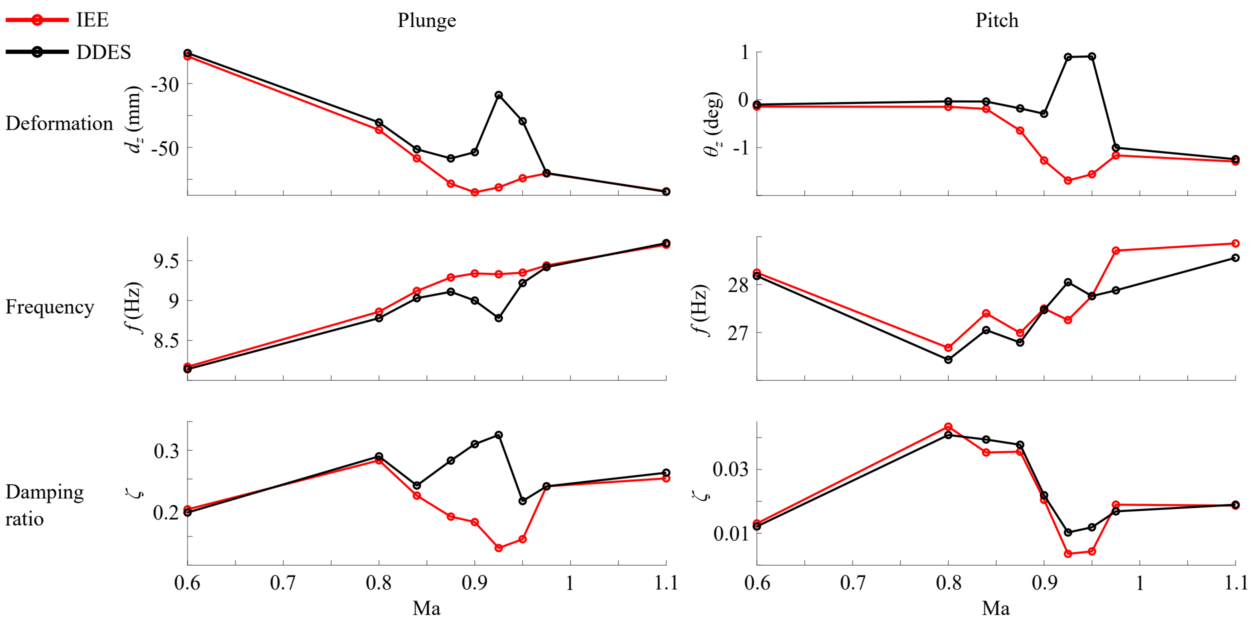

FIG. 9. The deformation, frequencies and damping ratios of the plunge and pitch for inviscid and viscous flow simulations at a constant free-stream static pressure of 94 kPa.

The time-averaged surface pressure coefficients at 65% of the wingspan are shown for different Mach numbers in Figure 10. The results from the simulations with the static deformation and those of the original rigid (undeformed) wing structure are compared for IEE and DDES. It is worth noting that there are very small low-frequency fluctuations in the converged results of the static simulations for $0.1s < t < 0.25s$ due to numerical errors, as displayed in Figure 8. Therefore, the static results discussed throughout this paper are averaged in time.

As can be seen in Figure 10, only at $Ma = 0.6$, IEE and DDES give the same results no matter if the wing structure is rigid, meaning that the viscous and FSI effects are negligible. As the Mach number increases up to $Ma = 0.8$, the results of the two methods are still similar, while the wing deformation affects the pressure distribution near the shock wave. For the Mach numbers above

0.8395, the differences caused by the viscous effects become noticeable at about 0.25 chord length and at the shock wave position, where the absolute values of the pressure at the suction side of the wing fall down. Meanwhile, the structure deformations also introduce differences, but the levels are much smaller than those caused by the viscous effects. Besides, the shock wave appears at $Ma = 0.8395$, and its position moves downstream as the Mach number increases. The position is almost at the trailing edge of the wing at $Ma = 0.975$ and 1.1.

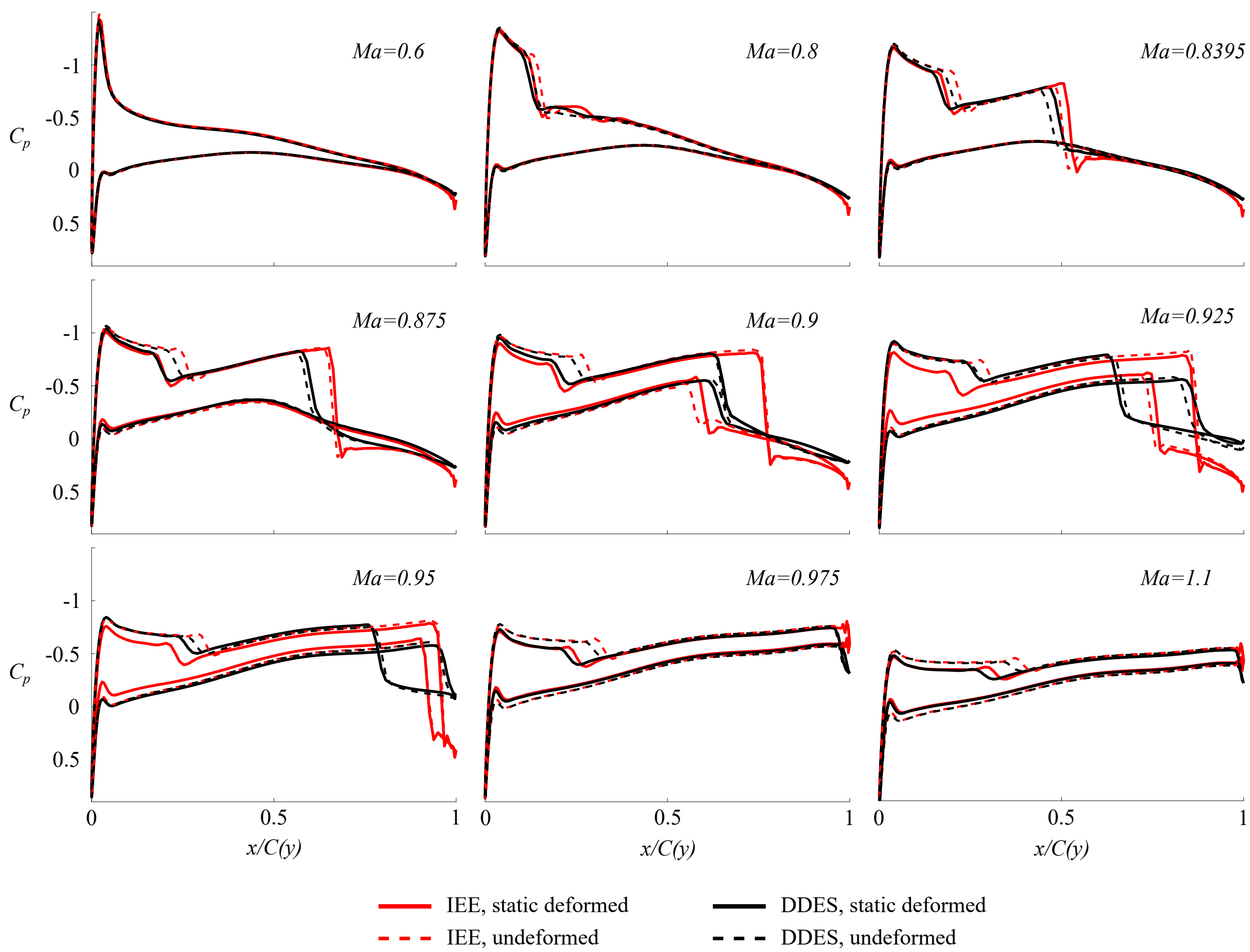

FIG. 10. Time-averaged surface pressure coefficients at the static deformation at the 65% wingspan at $Ma = 0.6 - 1.1$. The corresponding values of the undeformed wing are included for comparison.

The time-averaged surface pressure coefficients at 90% of the wingspan are shown in Figure 11. The phenomena are overall similar to those observed at 65% of the wingspan, but sudden pressure increase on the suction side is only obvious around the shock wave position for Ma below 0.95. The other increase at 0.25 chord length found for 65% of the wing span does not exist for the 90% position near the wing tip, although this increase is slightly shown at $Ma = 0.975$ and 1.1.

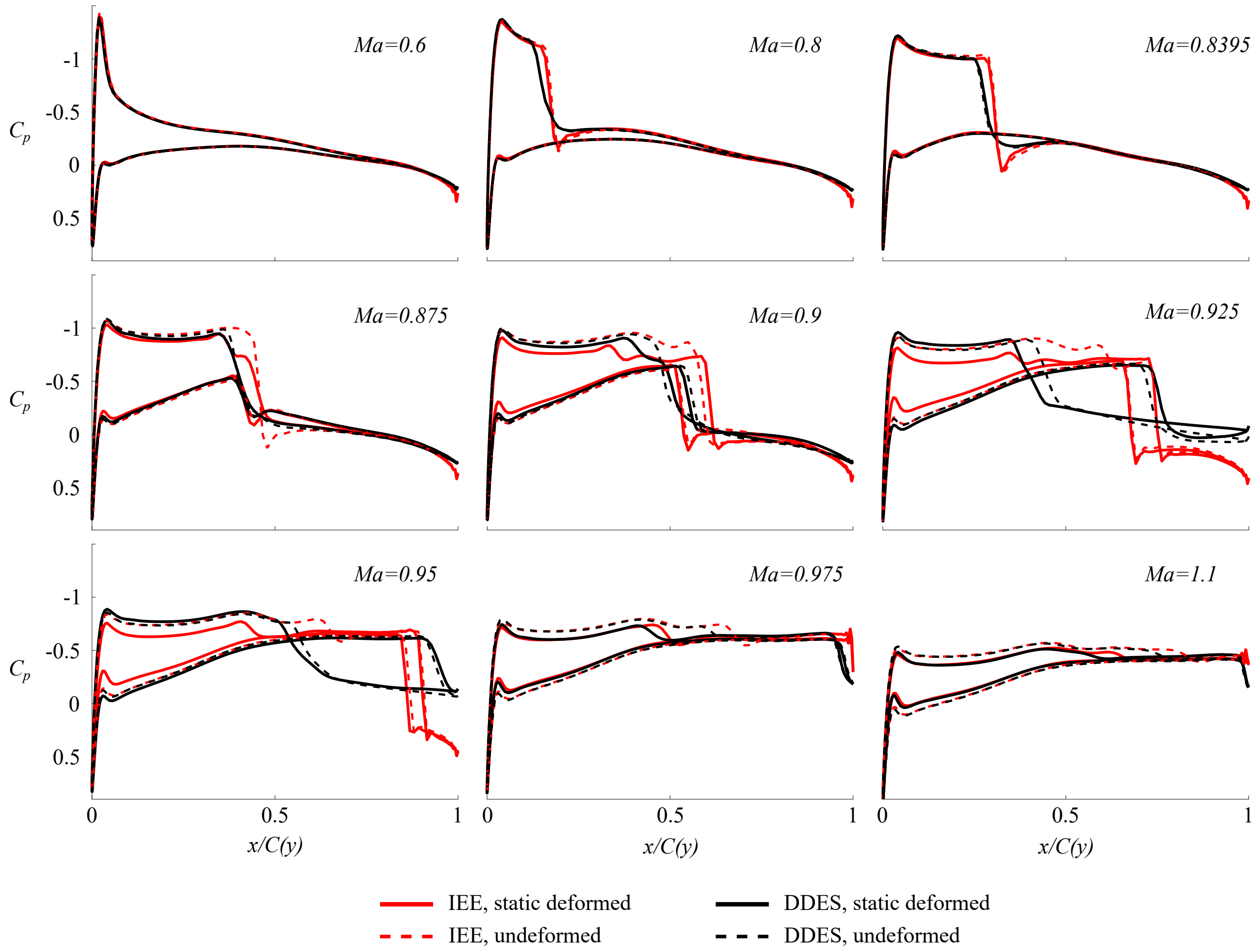

FIG. 11. Time-averaged surface pressure coefficients at the static deformation at the 90% wingspan at $Ma = 0.6 – 1.1$. The corresponding values of the undeformed wing are included for comparison.

The contours of the time-averaged pressure coefficients on the suction side of the wing are illustrated in Figure 12. A common phenomenon at $Ma = 0.8 – 1.1$ captured by both IEE and DDES is that a low pressure region is developed from the wing leading edge and grows along the spanwise direction from the wing root to tip. There is also a low pressure region at the smallest Mach number of 0.6, but the growth along the wingspan does not appear. These observations are in line with Figures 10 and 11, and it is clear that the viscosity affects the ending position of this low pressure region, where the pressure gets a significant increase.

Another common phenomenon seen in Figure 12 is the presence of the shock wave for the Mach numbers above 0.8395, although it is not well captured in the inviscid flow at $Ma = 0.975$ and 1.1. Moreover, in this Mach number range, IEE and DDES gives different shock wave positions along the wing span. The pressure distributions in the viscous and inviscid flows are the same at

$Ma = 0.6$, and slightly different at $Ma = 0.8$. Thus, the viscosity is effective in influencing the formation of the shock wave. The FSI is affected accordingly.

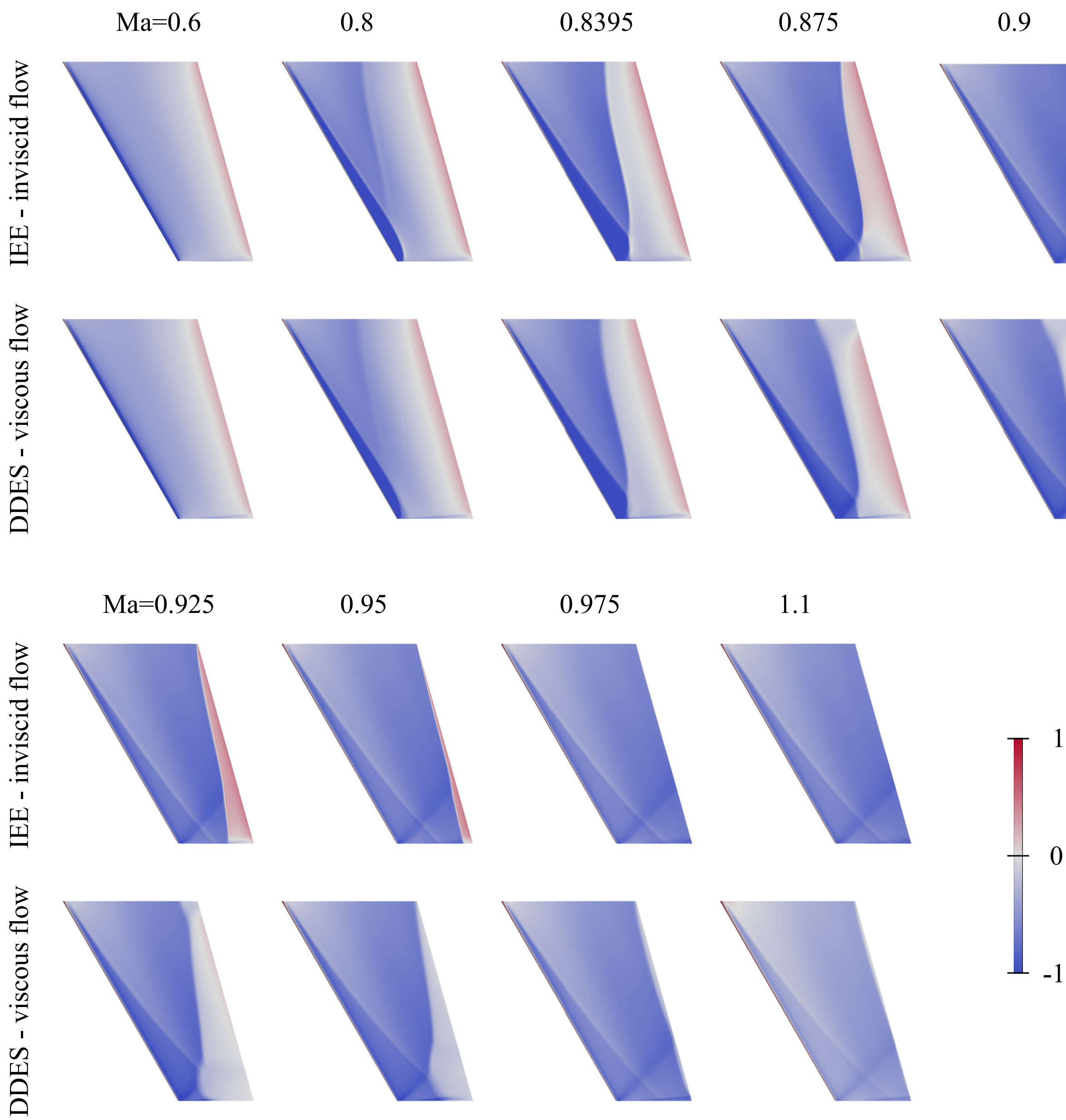

FIG. 12. Contours of the time-averaged surface pressure coefficients on the wing suction side, computed from the simulations with the static structural deformation.

Figure 13 shows the lift and drag coefficients, C_l and C_d, for the deformed and undeformed wings. IEE and DDES are compared to identify the effects of the viscosity. A significant drop in the lift is observed for the inviscid flow with IEE for $Ma > 0.8395$, due to the static aeroelastic deformation. However, for the viscous flow, the lift is similar for the undeformed and deformed wing up to $Ma = 0.95$, whereas there is a significant drop at Mach 0.975–1.1. An increase in the drag can be seen, which relates to the decreased lift. Besides, it is evident that the viscous effects are important at the transonic speeds for the lift prediction, not only in the case of an elastic wing but also for the rigid wing. The largest lift differences between the viscous and inviscid flows are found for the rigid wing. The viscosity consistently results in the shock wave positions further upstream, and the high pressure downstream the shock acts on a larger surface area.

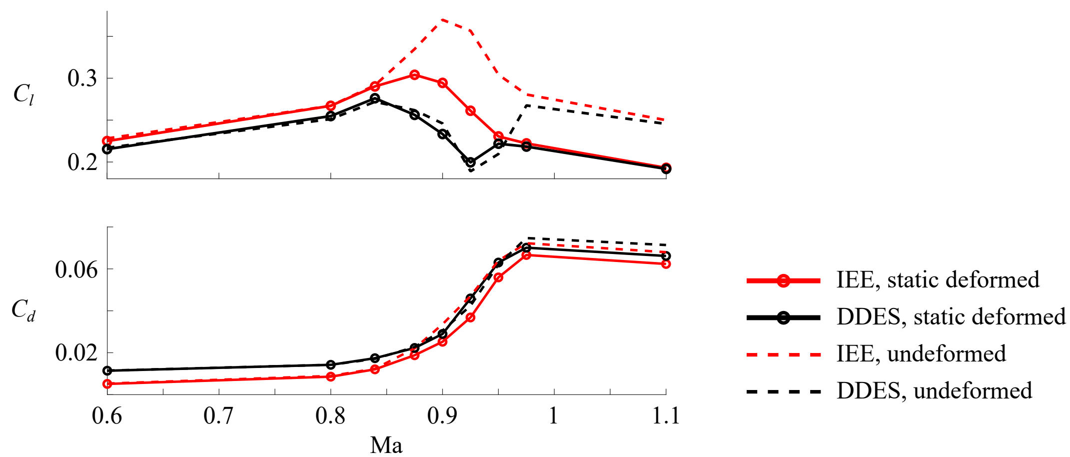

FIG. 13. The lift and drag coefficients, C_l and C_d, at the static deformation for inviscid and viscous flow. Dashed lines show corresponding quantities for the undeformed wing.

The analysis of the flow fields with the static deformation affirms the flow separation commencing at $Ma = 0.925$ and 0.95, but not at the other Mach numbers. The separation is restricted to the area adjacent to the wingtip. Figure 14 shows the time-averaged velocity field of the static structure deformation at 90% of the wingspan for Mach 0.925. A flow recirculation bubble can be seen in the region between the shock wave and the trailing edge. A vortex can also be seen downstream the trailing edge.

B. Flutter boundary prediction

Here, we discern the viscous effects using IEE and DDES that mathematically exclude and include the viscosity in the governing equation systems. Figure 15 shows plunge and pitch motions responding to two free-stream dynamic pressures at different Mach numbers, which are simulated using IEE (for the inviscid flow) and DDES (for the viscous flow). The larger dynamic pressure triggers structural responses increasing in time, whereas the smaller one leads to decaying struc-

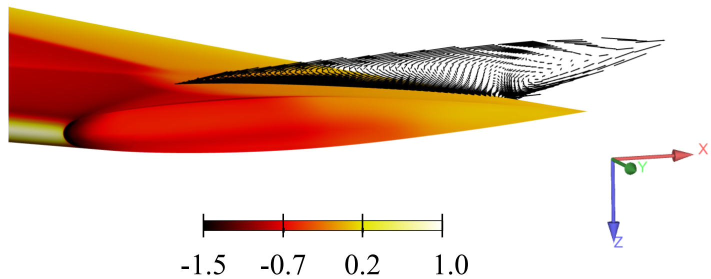

FIG. 14. The time-averaged velocity field at 90% of the wingspan at Mach 0.925 for the static structural deformation. The wing surface is coloured by the pressure coefficient.

tural responses. Both pressures between the inviscid and viscous flows are nearly identical up to $Ma = 0.8395$, and the discrepancies between the flows are less than 2.2%. However, the deviations between the flows increase rapidly when the Mach numbers are between $Ma = 0.8395$ and 0.925. At $Ma = 0.875$, the two pressures of the viscous flow are approximately 12% higher relative to those of the inviscid flow. The differences increase to 7% at $Ma = 0.9$, and approximately 53% at the Mach number of 0.925. Moreover, since the structural plunge and pitch amplitudes grow dramatically at the flutter boundary of $p_{dyn} = 227kPa$ at $Ma = 0.925$, the simulation diverges at $t = 0.55s$.

As the flow speed is increased from $Ma = 0.925$ to $Ma = 0.95$, the deviations of the pressures between the flows become smaller. A decreasing trend of the predicted deviations is observed when the Mach number further increases up to 1.1. At $Ma = 1.1$, the viscous effect is decreased, given that the pressures predicted with DDES are approximately 5% lower relative to those from IEE.

In a few cases such as $Ma = 0.975$ and 1.1 in Figure 15 for the smaller pressure, the structural dynamic responses increase initially for the first two peak amplitudes right after $t = 0.25s$, and subsequently decrease with positive damping. This behaviour is different from the other low Mach number cases, where a continuously decaying trend is observed.

The flutter boundary means the critical dynamic pressure, above which structural plunge and pitch responses become diverged in time. It is known that the critical dynamic pressure is dependent on the Mach number, while the viscous effects on the critical pressure are unclear. The critical dynamic pressure of the flutter boundary, as well as the characteristic frequency of the resultant structural responses, are shown at the different Mach numbers in Figure 16. The critical dynamic pressure is determined when plunge and pitch oscillations are retained constantly without decay-

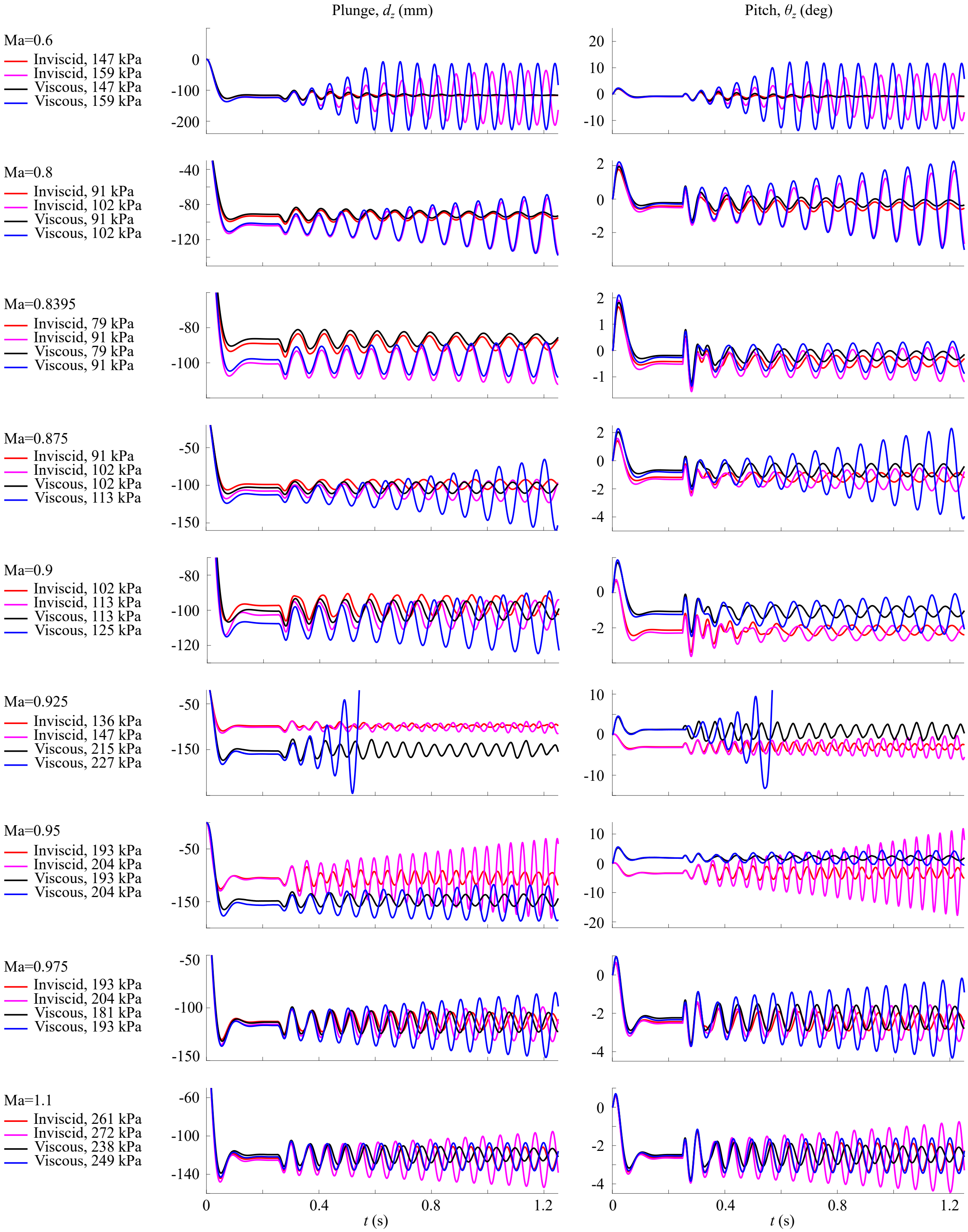

FIG. 15. The static (in $0 < t < 0.25$ s) and dynamic (in $0.25 < t < 1.25$ s) plunge and pitch responses of the wing structure subjected to the inviscid and viscous flows at Mach numbers 0.6–1.1 with different dynamic pressure p_{dyn}.

ing and increasing, that is, the damping ratio is zero. It is worth noting that when the flutter is triggered, the plunge and pitch exhibit the same characteristic frequency because of the coupling of these two modes. IEE and DDES gave nearly the same critical pressure and characteristic frequency from $Ma = 0.6$ to 0.8395, which are mostly in the subsonic regime. This suggests that the viscosity effect is insignificant to trigger the flutter in the subsonic flows. In contrast, remarkable differences between the results of the two methods are observed at $Ma = 0.925$. According to the static simulations illustrated in Figure 12, the methods provide obviously different predictions for the flow separation location and surface pressure distribution. Consequently, it is deduced that the dynamic structural responses to the flow surface force fluctuations are also influenced. Similar static surface pressure differences are also seen at $Ma = 0.95$. So the flutter frequency without considering the viscosity is different from that with the viscosity, although the critical pressure is occasionally identical.

As can be seen in Figure 16, the flutter critical pressure and frequency decrease with the Mach number for $Ma < 0.8395$. The overall trends turn to increasing at the larger Mach numbers, while an obvious increase is discerned at $Ma = 0.925$ due to the flow separation and significant changes in the surface pressure distribution indicated in Figure 12.

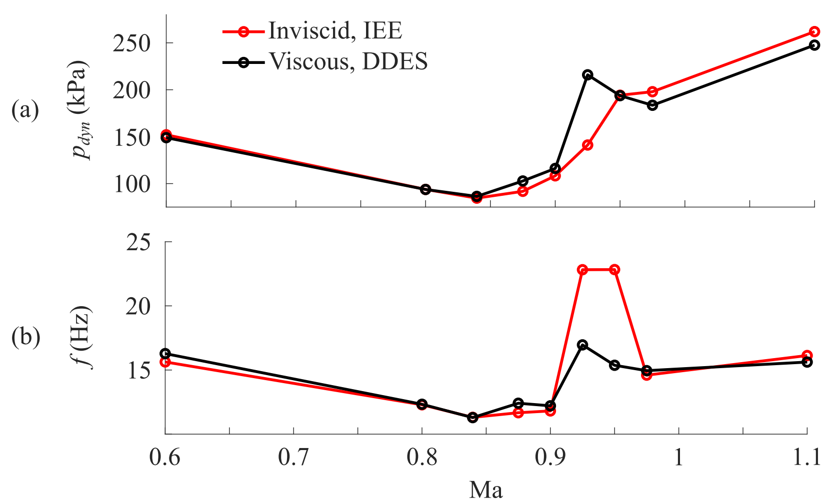

FIG. 16. (a) The critical dynamic pressure of the flutter boundary, and (b) the corresponding characteristic frequency of the plunge and pitch motions. IEE and DDES accounting for the inviscid and viscous flows, respectively.

C. Comparison of CFD methods

Cases 7, 8 and 9 at $Ma = 0.8395$ in Table III are simulated using all three CFD methods such as DDES, URANS and IEE. The static simulations are performed until $t = 0.25s$. Then, the converged solutions of the static simulations are used as the initial conditions for the dynamic simulations.

The static and dynamic plunge and pitch responses of Cases 7, 8 and 9 are displayed in Figure 17. The free-stream dynamic pressures are $p_{dyn} = 46$, 79 and $91\,kPa$, pertaining to comparatively fast decaying, slow decaying and increasing tendencies of the structural responses in time. The results of the viscous flows simulated using URANS an DDES are nearly the same, but they are different from the inviscid flows using IEE. This phenomenon indicates that the viscous effects are crucial for FSI at $Ma = 0.8395$, which is the critical Mach number bounding between the subsonic and transonic regimes as shown in Figure 16. Besides, the turbulence modelling techniques of DDES and URANS have negligible effects on FSI at this specific Mach number.

For the flows at the subsonic free-stream speeds below $Ma = 0.8395$, URANS and DDES give the same result since there is no flow separation near the walls. As the free-stream dynamic pressure increases, the structure deformation grows and results in fairly high local AOA. The implications are twofold: the separation commences more likely due to the increased AOA, and the shock wave is strengthened due to greater flow speed over the leading edge, which in turn may provoke the separation. Besides, increased free-stream dynamic pressure at constant Mach number and temperature can give rise to an increase in the density and thus the Reynolds number, which affects the boundary-layer growth and tendency towards the separation.

As revealed in the previous section, flow separation at static deformation for $Ma = 0.9250$ at the lowest dynamic pressure, i.e., Case 18. Moreover, the predicted flutter boundary is the most deviant at this Mach number, compared with all other Mach numbers, (see Figures 16 and 15). Furthermore, the structure deformations are also largest. Cases 21 and 22 are therefore deemed to be especially interesting to compare URANS and DDES. The plunge and pitch deformations obtained with these methods are shown in Figure 18. In Case 21 with $p_{dyn} = 215\ kPa$, the deformations from the URANS simulations diverge, while the results of DDES oscillate periodically. It means that URANS predicts lower damping. As p_{dyn} is increased to $227\ kPa$ in Case 22, both URANS and DDES produce diverging results. In other words, the critical p_{dyn} of the flutter boundary is underestimated by URANS, which is approximately $215\,kPa$, compared to around $227\,kPa$

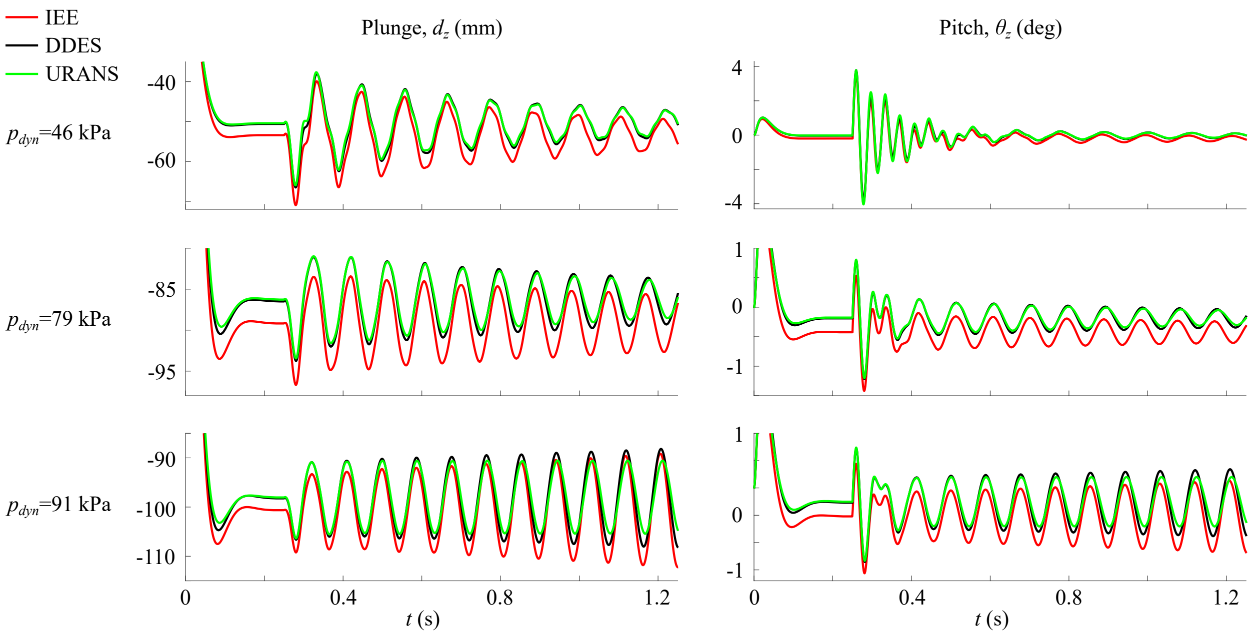

FIG. 17. Static ($0 < t < 0.25$ s) and dynamic ($0.25 < t < 1.25$ s) plunge and pitch responses in the inviscid and viscous flow simulations using IEE, DDES, and URANS at the Mach number of 0.8395 with different dynamic pressures p_{dyn}.

from DDES. The static plunges of the two methods are consistent, but the static pitches of URANS are negative and smaller than those from the other method.

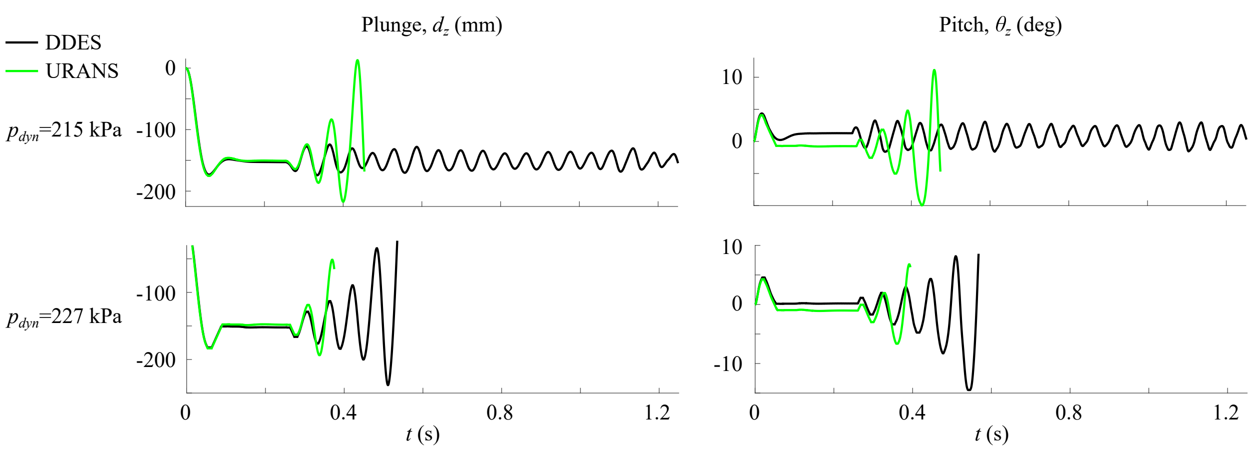

FIG. 18. The static ($0 < t < 0.25$ s) and dynamic ($0.25 < t < 1.25$ s) plunge and pitch responses in the viscous flows at $Ma = 0.925$ with different free-stream dynamic pressures p_{dyn}, simulated using DDES and URANS.

Contours of the time-averaged surface pressure coefficient in the dynamic simulations of Cases

21 and 22 at $Ma = 0.925$ are illustrated in Figure 19. DDES and URANS exhibits different distributions of the pressure and structure deformation, especially the position of the shock wave along the wing span. The negative pressure regions from URANS in both flow conditions are overall smaller than DDES, since the presence of the shock wave is delayed in the URANS simulations.

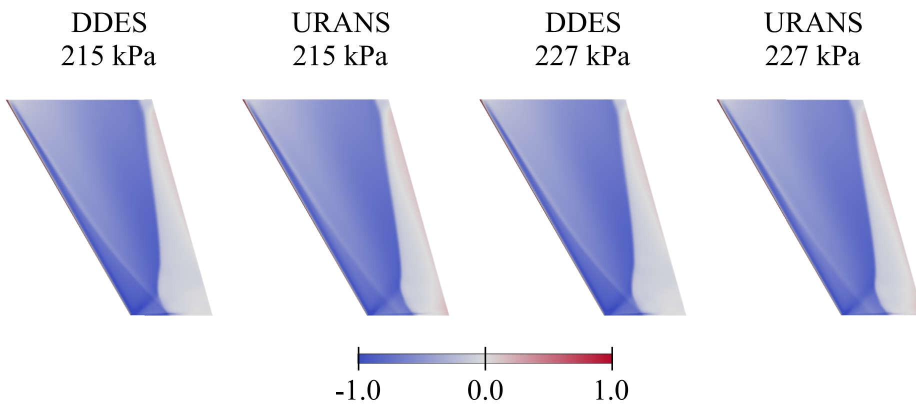

FIG. 19. Time-averaged surface pressure coefficient for the static deformation simulations at $Ma = 0.925$ in Case 21 of $p_{dyn} = 215\ kPa$ and Case 22 of 227 kPa, simulated using DDES and URANS.

Figure 20 shows the contours of the pressure recovery factor in the cutting plane at 90% of the wing span, which are computed in the static deformation simulations at $Ma = 0.925$ and $p_{dyn} = 215\ kPa$. The pressure recovery factor is defined as the local total pressure normalised by the free-stream total pressure. It can be seen in DDES and URANS that the factor undergoes a sharp change downstream of the middle of the airfoil. The sharp change is related to the flow separation, and it appears earlier in DDES than URANS. This phenomenon is consistent with the observation of the time-average surface pressure in the static deformation simuilation in Figure 19. The coupling between fluid and structure may play a role here. Since the shock wave appears slightly further upstream in DDES in comparison with URANS, the pitching moment obtained from the two methods are different. This results in an increased AOA. With the higher AOA, the shock wave moves further upstream, and the flow separation grows. This effect further increases the pitching moment. Therefore, the pitch in URANS is negative and diverged at the critical dynamic pressure of $215\,kPa$, which is smaller than $227\,kPa$ in DDES, as displayed in Figure 18.

FIG. 20. Contours of the pressure recovery factor in the cutting plane at 90% of the wingspan, obtained from the simulation of the static deformation subjected to the flow at $Ma = 0.925$ and $p_{dyn} = 215\ kPa$.

V. CONCLUSIONS

The effects of fluid viscosity and density on the aeroelastic prediction of the ONERA M6 wing are studied by utilising IEE and DDES with the SA turbulence model. In addition, a few selected cases are simulated with URANS. The flow speeds span from the subsonic to transonic regimes. Since the viscosity is considered in DDES and URANS but not in IEE, the viscous effects are discerned based on the comparison of these methods, especially between DDES and IEE in this paper. Viscous effects on static and dynamic structural responses are first examined by simulating Mach numbers ranging from 0.6–1.1, with a free-stream static pressure of 94 kPa.

The results evince the significance of the viscosity for the prediction of the aeroelastic at transonic speeds. Substantial differences in static and dynamic structural responses are found for Mach numbers ranging 0.875–0.95. The deformations resulting from the inviscid flow simulated with IEE are larger than those from the viscous flow of DDES, along with comparatively lower damping ratios. Moreover, the viscosity has minor effects at the subsonic speeds below $Ma = 0.8395$, as well as at the supersonic speed of $Ma = 1.1$ where both static and dynamic responses are nearly identical. Shock wave positions and transition pace from low to high surface pressure across the shock waves differ in the transonic region by dint of viscous effects. Hence, the pressure distribution, aerodynamic forces and moments differ, leading to different static and dynamic responses. The flow is attached at all Mach numbers except at 0.925 and 0.95 (Cases 18 and 23), as founded in the simulations of the static deformation. A URANS simulation is also undertaken for $Ma = 0.8395$ at the free-stream dynamic pressure of 94 kPa. The differences of structural responses between URANS and to DDES are not significant.

The flutter boundary (i.e., the critical free-stream dynamic pressure triggering the flutter) is obtained for each Mach number by gradually adjusting the free-stream static pressure, while maintaining free-stream temperature and velocity. As a consequence, the adjustment accounts for the increase of the free-stream density and dynamic pressure. DDES and IEE give nearly identical results of the flutter boundary for the Mach numbers smaller than 0.8395, suggesting that the viscous effects are negligible in the subsonic regime.

For the Mach numbers above 0.8395, compared to IEE, the flutter boundary in DDES is approximately 12% and 7% higher at $Ma = 0.875$ and 0.9, respectively, but 5% lower at $Ma = 1.1$. Especially at $Ma = 0.925$ where the flow separation is presented, the flutter boundary in DDES is approximately 53% higher. These discrepancies between the two methods indicate that the viscosity plays an important role in FSI in the transonic regime.

Based on the simulation results with the static deformation, the flow separation occurs at $Ma =$ 0.925 (Cases 21 and 22 with different free-stream static pressure), 0.95 (Cases 24 and 25 with different free-stream static pressure), and 0.9750 (Case 28). Since the separation is affected by the viscosity, the structural plunge and pitch deformations that response to the aerodynamic forces and moment are influenced by the viscosity accordingly. The comparatively larger separation in DDES may be caused by, or at least be exacerbated by a higher local AOA.

The turbulence simulation methods, DDES and URANS, are compared in terms of the flutter boundary. The differences between the methods are small at $Ma = 0.8395$. In contrast, the differences of the structural dynamic deformations are obvious at Mach 0.925. The static plunge deformations from the two methods are nearly the same, whilst the static pitch deformations from URANS is around one degree smaller than DDES. Moreover, URANS results in lower damping in the structural dynamic deformations. Hence, the flutter boundary obtained with this method is smaller than DDES.

ACKNOWLEDGMENTS

H.D.Y. obtained support of the computations/data handling that were enabled by resources provided by the Swedish National Infrastructure for Computing (SNIC) at Vera and Tetralith partially funded by the Swedish Research Council through grant agreement no. 2018-05973. Also, H.-D.Y. got support from the Chalmers foundation project on Hydro/Aerodynamics initiative.

REFERENCES

[1]H. Babinsky and J. K. Harvey, *Shock Wave-Boundary-Layer Interactions* (Cambridge University Press, 32 Avenue of the Americas, New York, NY 10013-2473, USA, 2011).

[2]J. Heeg, P. Chwalowski, D. Schuster, and M. Dalenbring, "Overview and lessons learned from the aeroelastic prediction workshop," 54th AIAA/ASME/ASCE/AHS/ASC Structures, Structural Dynamics, and Materials Conference (2013).

[3]E. H. Dowell, *A Modern Course in Aeroelasticity* (Springer, Gewerbestrasse 11, 63 30 Chamm Switzerland, 2022).

[4]H. D. Hodges and G. A. Pierce, *Introduction to Structural Dynamics and Aeroelasticity* (Cambridge University Press, 32 Avenue of the Americas, New York, NY 10013-2473, USA, 2011).

[5]D. G. Mabey, "A review of scale effects in unsteady aerodynamics," Prog. Aerospace Sci. **28**, 273–321 (1991).

[6]N. Durrani and N. Qin, "Comparison of rans, des and ddes results for onera m-6 wing at transonic flow speed using an in-house parallel code," 49th AIAA Aerospace Sciences Meeting (2011).

[7]P. Spalart and S. Allmaras, "A one-equation turbulence model for aerodynamic flows," La Recherche Aérospatiale **1**, 5–21 (1994).

[8]P. Spalart, S. Deck, M. Shur, K. Squires, M. K. Strelets, and A. Travin, "A new version of detached-eddy simulation, resistant to ambiguous grid densities," Theory of Computational Fluid Dynamics **20**, 181–195 (2006).

[9]V. Schmitt and F. Charpin, "Pressure distributions on the onera-m6-wing at transonic mach numbers, experimental data base for computer program assessment." Report of the Fluid Dynamics Panel Working Group 04, AGARD AR 138 (1979).

[10]P. Eliasson, "Edge, a navier–stokes solver for unstructured grids," finite volumes for complex applications," CP849 **III**, 527–534 (2002).

[11]P. Eliasson and P. Weinerfelt, "Recent applications of the flow solver edge," 7th Asian CFD Conference (2007).

[12]Palombo, C. L., "Development and validation of an improved wall-function boundary condition for computational aerodynamics," (2021), master thesis, Royal Institute of Technology, Stockholm, Sweden.

[13]G. F. Franklin, J. D. Powell, and A. Emami-Naeini, *Feedback Control of Dynamic Systems* (Pearson Prentice Hall, Upper Saddle River, New Jersey, 07458, 2010).